ARTICLE NO. 79-0130R

# Numerical Simulation of Steady Supersonic Viscous Flow

Lewis B. Schiff* and Joseph L. Steger†
*NASA Ames Research Center, Moffett Field, Calif.*

**A noniterative, implicit, space-marching, finite-difference algorithm is developed for the steady thin-layer, Navier-Stokes equations in conservation law form. The numerical algorithm is applicable to steady supersonic viscous flow over bodies of arbitrary shape. Computed results from two- and three-dimensional versions of the numerical algorithm are in good agreement with those obtained from more costly time-marching techniques.**

## I. Introduction

FOR steady, supersonic, high Reynolds number viscous flows about configurations with moderate axial geometry variation, a substantial reduction in both computational effort and required storage over those of time-dependent numerical methods can be achieved by utilizing the parabolized Navier-Stokes equations. The parabolized Navier-Stokes equations are obtained by 1) neglecting the unsteady terms as well as the streamwise viscous diffusion terms within the Navier-Stokes equations, and 2) by modifying the streamwise convective flux vector to permit stable time-like marching of the equations downstream from initial data. The resulting equations are commonly referred to as the parabolized Navier-Stokes equations because they are parabolic-like with respect to the downstream marching coordinate. Computational efficiency and reduced storage requirements are obtained because the parabolized equations are solved by advancing an initial plane of data in space, rather than by advancing an initial cube of data in time, as is done for the full Navier-Stokes equations. The parabolized Navier-Stokes approximation has been employed by numerous researchers for both external flows (c.f., Refs. 1-6) and internal flows (c.f., Refs. 7-12).

In the present paper we present a noniterative, implicit, finite-difference algorithm, analogous to that developed by Beam and Warming[13,14] for unsteady flow, for the solution of the parabolized Navier-Stokes equations. The algorithm is conservative, of second-order accuracy in the marching direction, and can have second- or fourth-order accuracy in the transverse directions.

In Sec. II we detail the parabolized Navier-Stokes approximation and the numerical algorithm for steady two-dimensional flow. Section II also contains sample computed results and a discussion of the stability of the present method. In Sec. III, we outline the extension of the method to steady three-dimensional flow, and present sample results that demonstrate the accuracy and versatility of the resulting factored algorithm.

## II. Two-Dimensional Flow

Discussion of the parabolized Navier-Stokes approximation and illustration of the numerical algorithm are facilitated if we first consider the case of steady two-dimensional flow. The extension to steady three-dimensional flow is given in Sec. III.

Presented as Paper 79-0130 at the AIAA 17th Aerospace Sciences Meeting, New Orleans, La., Jan. 15-17, 1979; submitted April 27, 1979; revision received March 18, 1980. This paper is declared a work of the U.S. Government and therefore is in the public domain.

Index categories: Computational Methods; Supersonic and Hypersonic Flow.

*Research Scientist, Aerodynamic Research Branch. Member AIAA.

†Research Scientist; presently, Professor, Stanford University, Stanford, Calif. Member AIAA.

### A. Governing Equations

*1. Generalized Coordinate Transformation*

In order to accommodate body-conforming coordinates, we introduce new independent spatial variables which transform the physical $x$, $z$ plane surrounding the body (Fig. 1a) into a rectangular $\xi$, $\zeta$ computational plane (Fig. 1b). The transformation, of the form

$$\left.\begin{aligned}\xi &= \xi(x) = \text{streamwise coordinate}\\ \zeta &= \zeta(x,z) = \text{normal coordinate}\end{aligned}\right\} \tag{1}$$

maps the body surface onto $\zeta = 0$. This transformation both simplifies the application of surface boundary conditions and makes possible the approximation of neglecting streamwise

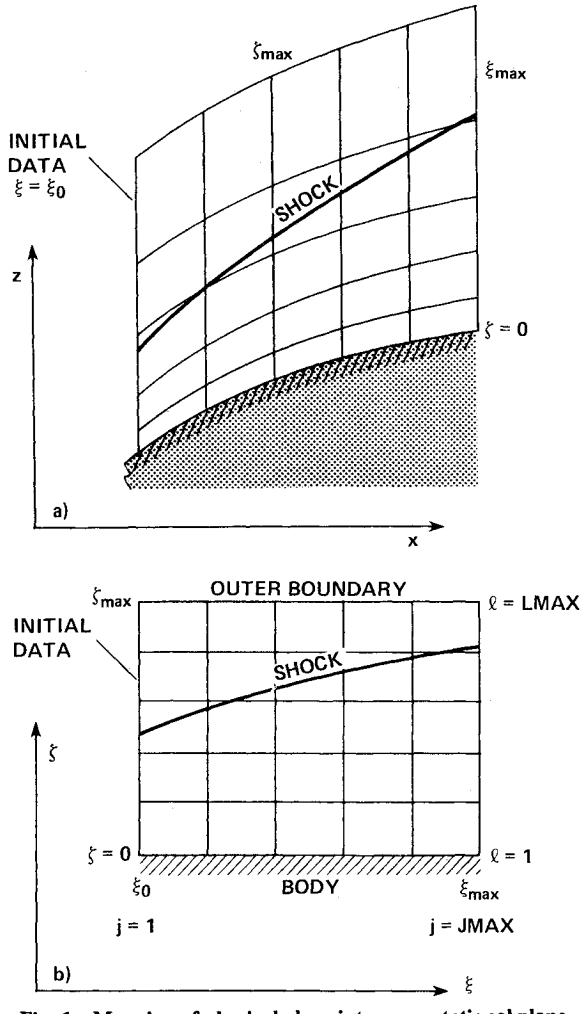


**Fig. 1 Mapping of physical plane into computational plane.**

viscous terms in high Reynolds number flow. The Jacobian of the transformation is:

$$J=\xi_x\zeta_z=1/(x_\xi z_\zeta) \tag{2}$$

and the metric derivatives, $\xi_x$, $\zeta_x$, etc., in the computational plane, are related to those in the physical plane, $x_\xi$, $z_\xi$, etc., by

$$\xi_x=Jz_\zeta \quad \xi_z=0 \quad \zeta_x=-Jz_\xi \quad \zeta_z=Jx_\xi \tag{3}$$

In this paper, we consider $\xi$ to be $\xi(x)$ only. Thus, vertical lines in the physical plane map into vertical lines of the computational plane.

### 2. *Gasdynamic Equations*

The first step in obtaining the parabolized Navier-Stokes equations is to neglect all "streamwise" derivatives, $\partial/\partial\xi$, within the viscous terms. This approximation is physically justified for high Reynolds number flow past body-conforming coordinates by using the usual arguments of boundary-layer theory. (See also Rudman and Rubin[15] or Davis[16] for related hypersonic viscous-flow analysis.) Neglect of the streamwise viscous terms is necessary to prevent exponential growth in marching the equations in $\xi$, that is, in order to mathematically change the nature of Eq. (4) from elliptic-like to parabolic-like type with respect to the $\xi$ coordinate. The transformed Navier-Stokes equations in strong conservation form can, upon neglecting the streamwise derivatives, be written as (c.f. Refs. 17, 18)

$$\frac{\partial\hat{E}}{\partial\xi}+\frac{\partial\hat{G}}{\partial\zeta}=\frac{1}{Re}\frac{\partial\hat{S}}{\partial\zeta} \tag{4}$$

where

$$\hat{E}=\frac{\xi_x}{J}E=\frac{1}{J}\begin{bmatrix}\rho U\\ \rho uU+\xi_x p\\ \rho wU\\ (e+p)U\end{bmatrix},\quad \hat{q}=\frac{1}{J}q=\frac{1}{J}\begin{bmatrix}\rho\\ \rho u\\ \rho w\\ e\end{bmatrix}$$

$$\hat{G}=\frac{\zeta_x}{J}E+\frac{\zeta_z}{J}G=\frac{1}{J}\begin{bmatrix}\rho W\\ \rho uW+\zeta_x p\\ \rho wW+\zeta_z p\\ (e+p)W\end{bmatrix}$$

and the contravariant velocity components $U$, $W$ are defined in terms of the Cartesian velocity components $u$, $w$ as

$$\left.\begin{aligned}U&=\xi_x u\\ W&=\zeta_x u+\zeta_z w\end{aligned}\right\} \tag{5}$$

The internal energy of the gas, $e_i$, is defined in terms of the conservative variables as

$$e_i=(e/\rho)-0.5(u^2+w^2) \tag{6}$$

and for a perfect gas with ratio of specific heats $\gamma$, the equation of state is:

$$p/\rho=(\gamma-1)e_i=a^2/\gamma \tag{7}$$

In Eqs. (4-7), the Cartesian velocity components $u$, $w$ are made nondimensional with respect to $a_\infty$ (the freestream speed of sound), density $\rho$ is normalized by $\rho_\infty$, and total energy $e$ is referenced to $\rho_\infty a_\infty^2$.

The viscous term $\hat{S}$ in Eq. (4) is:

$$\hat{S}=\frac{1}{J}\begin{bmatrix}0\\ \mu(\zeta_x^2+\zeta_z^2)u_\zeta+(\mu/3)(\zeta_x u_\zeta+\zeta_z w_\zeta)\zeta_x\\ \mu(\zeta_x^2+\zeta_z^2)w_\zeta+(\mu/3)(\zeta_x u_\zeta+\zeta_z w_\zeta)\zeta_z\\ (\zeta_x^2+\zeta_z^2)[(\mu/2)(u^2+w^2)_\zeta\\ \quad+\kappa Pr^{-1}(\gamma-1)^{-1}(a^2)_\zeta]\\ \quad+(\mu/3)(\zeta_x u+\zeta_z w)(\zeta_x u_\zeta+\zeta_z w_\zeta)\end{bmatrix} \tag{8}$$

In obtaining Eq. (8), use has been made of the Stokes hypothesis, $\lambda=-2\mu/3$, where $\lambda$ and $\mu$ are the coefficients of viscosity. Also, $\kappa$ is the coefficient of thermal conductivity, $Re$ is the freestream Reynolds number, and $Pr$ is the freestream Prandtl number. For turbulent flow computations, the eddy-viscosity model described by Baldwin and Lomax[19] is employed.

### 3. *Boundary Conditions*

Surface boundary conditions for Eq. (4) are simplified because the body surface has been mapped onto $\zeta=0$ (see Fig. 1). The steady no-slip condition is simply given by $U=W=0$. The pressure on the body surface can be determined from the $\zeta$ momentum equation evaluated at the wall. However, a simplified boundary condition, $\partial p/\partial\zeta=0$, is consistent with restrictions to be placed on the governing equations in order to maintain a stable streamwise marching procedure. The surface density is obtained from the equation of state using the found surface pressure and a specification of either the wall temperature or temperature gradient.

In the present computations, no provision has been made for fitting the bow shock wave. Instead, the outer edge of the computational region, $\zeta=\zeta_{\max}$, is chosen to extend into the undisturbed freestream beyond the shock layer, and the bow shock is captured.

A solution consistent with the parabolized Navier-Stokes approximation must be supplied as initial data. The initial data must be those of supersonic external flow, and the streamwise component of velocity must be everywhere positive.

### 4. *Jacobian Matrices of the Flux Vectors*

Jacobian matrices of the flux vectors are needed in our development of both the parabolized Navier-Stokes equations and in the implicit marching algorithm to be described later.

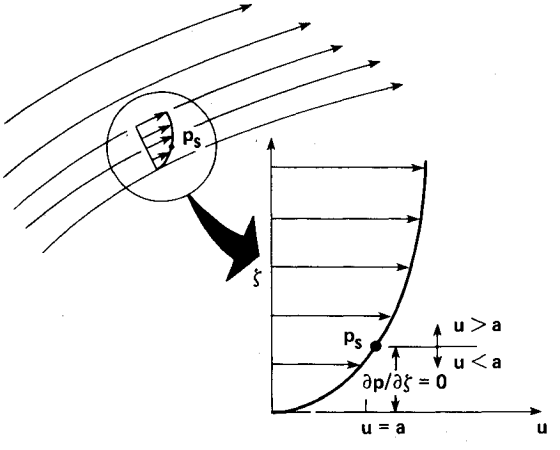


**Fig. 2 Schematic of sublayer approximation showing $p_s$ impressed from above.**

The Jacobian matrices $\hat{A} \equiv [\partial \hat{E}/\partial \hat{q}]$ and $\hat{C} = [\partial \hat{G}/\partial \hat{q}]$ can be written as

$$\hat{A} = \xi_x A, \quad \hat{C} = \zeta_x A + \zeta_z C \tag{9}$$

in terms of the Jacobian matrices of the Cartesian flux vectors $A \equiv [\partial E/\partial q]$ and $C \equiv [\partial G/\partial q]$. The matrices $A$ and $C$ are defined in Refs. 20 and 21. Likewise, the Jacobian matrix operator $\hat{M}$ for the viscous term is defined there.

The Cartesian flux vectors $E$ and $G$ are homogeneous functions of degree one in $q$. As a consequence, they possess the identities

$$E = Aq \quad G = Cq \tag{10}$$

The homogeneous property also extends to the generalized flux vectors, that is,

$$\hat{E} = \hat{A}\hat{q} \quad \hat{G} = \hat{C}\hat{q} \tag{11}$$

### B. Parabolized Navier-Stokes Approximation

#### 1. *Conditions for Stable Marching*

As alluded to in the introduction, the parabolized Navier-Stokes approximation for steady supersonic external flow employs two main assumptions: 1) the viscous terms in the marching direction $\xi$ (which we loosely refer to as streamwise) are negligible; and 2) the streamwise convective flux derivative has positive timelike behavior (discussed below) with respect to the remaining spatial derivatives. The first approximation is justified for high Reynolds number flow and body-conforming coordinates and has been discussed previously. The second assumption is the most difficult restriction to impose on the parabolized Navier-Stokes equations. With the Navier-Stokes equations arranged as in Eq. (4), by positive timelike behavior in $\xi$ we mean that the Jacobian matrix $A$ has positive eigenvalues. Although we oversimplify the analysis,[21] the restriction that $A$ has positive eigenvalues is required in inviscid flow for the equations to be hyperbolic and it is needed in viscous flow if positive viscosity is to cause damping in the marching direction. Insofar as the viscous flow near a no-slip wall is subsonic, at least one eigenvalue of $A$, the $u-a$ root, will be less than zero. Consequently, the solution can grow exponentially with marching unless this negative root is suppressed (see Ref. 21 for details).

#### 2. *The Subsonic Layer-Model*

Two observations are now made. The first is that if pressure can be specified in the flux vector $E$, that is, the given $p$ is not a function of $q$, then the sound speed contribution to the eigenvalues of $[\partial E/\partial q] = A$ is removed. In this way the eigenvalues of $A$ remain positive as long as $u > 0$. The second observation is that for high Reynolds number viscous flow, pressure is approximately constant through the thin subsonic viscous sublayer near the wall. Indeed, according to boundary-layer theory, for high Reynolds number flow the approximation $\partial p/\partial n = 0$ is valid over the entire thickness of the viscous layer. Thus, this approximation is even more apropos over just the subsonic portion of the viscous layer.

Although developed under a different formalism, these observations form the basis of the parabolized Navier-Stokes approximation that Rubin and Lin[2,3] term the sublayer approximation. In our development of the subsonic layer (i.e., sublayer) approximation, we begin by defining a new streamwise flux vector $\hat{E}_s$ given by

$$\hat{E}_s = \frac{\xi_x}{J} E_s = \frac{\xi_x}{J} \begin{bmatrix} \rho u \\ \rho u^2 + p_s \\ \rho u w \\ u(e + p_s) \end{bmatrix} \tag{12}$$

where $p_s = (\gamma - 1)\,[e - 0.5\rho\,(u^2 + w^2)]$ for supersonic flow $u > a\,(1 + \epsilon_s)$ and $p_s$ is defined from $\partial p/\partial \zeta = 0$ for subsonic flow $u < a\,(1 + \epsilon_s)$. Here we assume that $\zeta$ is effectively normal to the surface, and $\epsilon_s$ is a small positive number picked such that $u \neq a$ and $A^{-1}$ exists.

A schematic of how $p_s$ is evaluated is given in Fig. 2. The essential idea is that for points within the subsonic viscous sublayer, $p_s$ is not evaluated from the local flow variables, but is taken from the adjacent supersonic flow. Throughout the subsonic layer, it is assumed that $p_s \neq p_s(q)$, where $q$ is the local vector of dependent variables. Of course, $p_s$ is related to $q$ in the adjacent supersonic region.

The Jacobian matrix, $A_u \equiv [\partial E_s/\partial q]$ where $p_s$ is specified, is given by

$$A_u = \begin{bmatrix} 0 & 1 & 0 & 0 \\ -u^2 & 2u & 0 & 0 \\ -uw & w & u & 0 \\ -u(e+p_s)/\rho & (e+p_s)/\rho & 0 & u \end{bmatrix} \tag{13}$$

and has eigenvalues $\sigma(A_u) = u, u, u, u$, which are positive if $u > 0$. By using frozen coefficient analysis, it is shown in Ref. 21 that Eq. (4) should be stable for marching in $\xi$ if $E$ is replaced by $E_s$. Indeed, the vector $E_s$ was originally constructed from similarity transformations so that $A_u$ has the eigenvalues of $u$ (see Ref. 20 for related work).

Summarizing, the parabolized Navier-Stokes equations with the sublayer approximation can be expressed as

$$\frac{\partial \hat{E}_s}{\partial \xi} + \frac{\partial \hat{G}}{\partial \zeta} = \frac{1}{Re}\frac{\partial \hat{S}}{\partial \zeta} \tag{14}$$

where $\hat{E}_s$ is defined by Eq. (12), and the equations are stable for marching in $\xi$ when $u > 0$. The relation of Eq. (14) to past work is discussed in Ref. 21.

### C. Development of the Numerical Algorithm

A fully implicit, noniterative, finite-difference algorithm is constructed for the parabolized Navier-Stokes equations with the sublayer approximation. The difference equations are treated in vector form and their solution requires a block tridiagonal inversion at each marching step. Figure 1 indicates the extent of the computational domain and the definition of the indices $j$ and $\ell$.

#### 1. *Difference Operators*

An implicit, finite-difference scheme for Eq. (14) is constructed by selecting difference operators that would be stable for a model problem of diffusion and convection. The following difference approximations are selected for the inviscid flux vectors

$$\left(\frac{\partial \hat{E}_s}{\partial \xi}\right)^{j+1} \simeq \frac{(\hat{E}_s^{j+1} - \hat{E}_s^{j}) - \alpha(\hat{E}_s^{j} - \hat{E}_s^{j-1})}{(1-\alpha)\Delta\xi} + O(\Delta\xi)^{1+3\alpha} \tag{15}$$

where $\alpha = 0$ or $\frac{1}{3}$ for first- or second-order accuracy, and

$$\frac{\partial \hat{G}}{\partial \zeta} \simeq \delta_\zeta \hat{G} = \frac{\hat{G}_{\ell+1} - \hat{G}_{\ell-1}}{2\Delta\zeta}, \quad O(\Delta\zeta)^2 \tag{16}$$

Each term of the viscous flux vector $\partial_\zeta \hat{S}$ is of the form $\partial_\zeta(\phi \partial_\zeta \psi)$ and is differenced as

$$\delta_\zeta \phi \delta_\zeta \psi = \frac{(\phi_{\ell+1} + \phi_\ell)(\psi_{\ell+1} - \psi_\ell) - (\phi_\ell + \phi_{\ell-1})(\psi_\ell - \psi_{\ell-1})}{2\Delta\zeta^2} \tag{17}$$

Applying these operators to Eq. (14) gives

$$\frac{(\hat{E}_s^{j+1}-\hat{E}_s^j)-\alpha(\hat{E}_s^j-\hat{E}_s^{j-1})}{(1-\alpha)\Delta\xi}+\left(\delta_\zeta\hat{G}^{j+1}-\frac{1}{Re}\delta_\zeta\hat{S}^{j+1}\right)=0 \tag{18}$$

This choice of difference operators is unconditionally stable for the model initial-value problem in $\xi$

$$\frac{\partial u}{\partial\xi}\pm\frac{\partial u}{\partial\zeta}=\frac{\partial^2 u}{\partial\zeta^2} \tag{19}$$

Because $A$ or $A_u$ has positive real roots, we expect the difference equations represented by Eq. (18) to be unconditionally linear stable.

*2. Local Linearizations*

To avoid solving a nonlinear system of equations at each step in $\xi$, the flux vectors of Eq. (18) at $j+1$ are replaced by local linearizations about $j$. The local linearizations are defined as

$$E^{j+1}\simeq E^j+A^j(q^{j+1}-q^j)=A^jq^{j+1} \tag{20a}$$

$$G^{j+1}\simeq G^j+C^j(q^{j+1}-q^j)=C^jq^{j+1} \tag{20b}$$

$$\hat{G}^{j+1}\simeq(\zeta_x^{j+1}A^j+\zeta_z^{j+1}C^j)\hat{q}^{j+1}=\tilde{C}^j\hat{q}^{j+1} \tag{21a}$$

$$\hat{S}^{j+1}\simeq\tilde{S}^j+\tilde{M}^j(\hat{q}^{j+1}-\hat{q}^j)=\tilde{S}^j+\tilde{M}^j\hat{q}^{j+1} \tag{21b}$$

where all of the approximations are $0(\Delta\xi)^2$ and we have used the homogeneous property, Eq. (10). The Jacobian matrices $\hat{A}$, $\hat{C}$, and $\hat{M}$ are given in Ref. 21. Note that ($\tilde{}$) indicates that the matrices $\tilde{C}^j$, $\tilde{M}^j$ and the vector $\tilde{S}^j$ are evaluated using variables $\hat{q}$ at $j$ and metric quantities at $j+1$ [cf., Eq. (21a)].

The special flux vector $E_s$, $u<a$, has the functional form $E_s=E_s(q,p_s)$ and locally linearizes as

$$E_s^{j+1}\simeq E_s^j+\left[\frac{\partial E_s}{\partial q}\right]^j(q^{j+1}-q^j)+\left(\frac{\partial E_s}{\partial p_s}\right)^j(p_s^{j+1}-p_s^j)$$

$$\simeq A_u^jq^{j+1}+p_s^{j+1}\mathcal{P}^j \tag{22}$$

where $A_u$ is previously defined [Eq. (13)] while $\mathcal{P}$ is the vector $\mathcal{P}=(0,1,0,u)^t$. The quantity $p_s^{j+1}$ is also unknown, so we extrapolate

$$p_s^{j+1}=p_s^j+\beta(p_s^j-p_s^{j-1})+0(\Delta\xi)^{1+\beta} \tag{23}$$

where $\beta=0$ or 1 for first- or second-order accurate extrapolation. We remark that we have only exercised the $\beta=0$ option because the error of the first-order approximation, confined to the thin sublayer, has not been significant in our test calculations.

The linearization of $\hat{E}_s^{j+1}$ for either supersonic or subsonic flow can thus be expressed as

$$\hat{E}_s^{j+1}=\tilde{A}_s^j\hat{q}^{j+1}+\left(\frac{\xi_x}{J}\right)^{j+1}E_p^j \tag{24}$$

where

$$\tilde{A}_s^j=\tilde{A}^j=\xi_x^{j+1}A^j,\quad E_p^j=0$$

in supersonic regions, $u>a$, and

$$\tilde{A}_s^j=\tilde{A}_u^j\equiv\xi_x^{j+1}A_u^j,\quad E_p^j=[p_s^j+\beta(p_s^j-p_s^{j-1})]\mathcal{P}^j$$

in subsonic regions, $u<a$.

If only $\hat{E}_s^{j+1}$ is locally linearized, the three-point backward difference operator becomes first order and nonconservative. That is, for $\alpha=\frac{1}{3}$

$$\partial_\xi\hat{E}_s^{j+1}\simeq$$

$$\frac{[\tilde{A}_s^j\hat{q}^{j+1}+(\xi_x/J)^{j+1}E_p^j+0(\Delta\xi)^2-\hat{E}_s^j]-\alpha(\hat{E}_s^j-\hat{E}_s^{j-1})}{(1-\alpha)\Delta\xi} \tag{25}$$

is $0(\Delta\xi)^2/[(1-\alpha)(\Delta\xi)]=0(\Delta\xi)$ and is nonconservative. However, if $\hat{E}_s^j$ is also locally linearized, the lowest-order linearization error will be subtracted off; that is,

$$\partial_\xi\hat{E}_s^{j+1}\simeq\{[\tilde{A}_s^j\hat{q}^{j+1}+(\xi_x/J)^{j+1}E_p^j+0(\Delta\xi)^2-\tilde{A}_s^{j-1}\hat{q}^j$$

$$-(\xi_x/J)^jE_p^{j-1}-0(\Delta\xi)^2]-\alpha(\hat{E}_s^j-\hat{E}_s^{j-1})\}/[(1-\alpha)\Delta\xi] \tag{26}$$

The difference approximation, Eq. (26), is $0(\Delta\xi)^2$ and is a conservative operator. Even if only first-order accuracy is required in $\xi$, $\alpha=0$ above, it is still necessary to linearize each term of the difference $\hat{E}_s^{j+1}-\hat{E}_s^j$ in order to maintaina conservative differencing for shock-capturing purposes.

*3. Delta Form Algorithm*

Applying the local linearizations and adding a fourth-order dissipation term to Eq. (18) results in

$$(\tilde{A}_s^j\hat{q}^{j+1}-\tilde{A}_s^{j-1}\hat{q}^j)+(1-\alpha)\Delta\xi(\delta_\zeta\tilde{C}^j-Re^{-1}\delta_\zeta\tilde{M}^j)\hat{q}^{j+1}$$

$$=(1-\alpha)\Delta\xi Re^{-1}\delta_\zeta\tilde{S}^j+\alpha(\hat{E}_s^j-\hat{E}_s^{j-1})$$

$$-[(\xi_x/J)^{j+1}E_p^j-(\xi_x/J)^jE_p^{j-1}]+\mathfrak{D}\hat{q}^j \tag{27}$$

The fourth-order dissipation term has the form

$$\mathfrak{D}\hat{q}^j=\epsilon_e\tilde{A}_s^j(J^{-1})^j(\nabla_\zeta\Delta_\zeta)^2(J\hat{q})^j \tag{28}$$

and is added to suppress high-frequency oscillations. Here

$$(\nabla_\zeta\Delta_\zeta)^2q_\ell^j=q_{\ell+2}^j-4q_{\ell+1}^j+6q_\ell^j-4q_{\ell-1}^j+q_{\ell-2}^j \tag{29}$$

If $\alpha=0$, linear-stability analysis of the dissipation term alone indicates that $\epsilon_e$ must be less than 1/8.

Finally, the difference equations are put into delta form by subtracting $[\tilde{A}_s^j+(1-\alpha)\Delta\xi(\delta_\zeta\tilde{C}^j-Re^{-1}\delta_\zeta\tilde{M}^j)]\hat{q}^j$ from both sides of the equations. The finished form of the numerical differencing algorithm is then

$$[\tilde{A}_s^j+(1-\alpha)\Delta\xi(\delta_\zeta\tilde{C}^j-Re^{-1}\delta_\zeta\tilde{M}^j)](\hat{q}^{j+1}-\hat{q}^j)$$

$$=-(\tilde{A}_s^j-\tilde{A}_s^{j-1})\hat{q}^j+\alpha(\hat{E}_s^j-\hat{E}_s^{j-1})-(1-\alpha)\Delta\xi$$

$$\times\{\delta_\zeta[\zeta_x^{j+1}(E/J)^j+\zeta_z^{j+1}(G/J)^j]-Re^{-1}\delta_\zeta\tilde{S}^j\}$$

$$-[(\xi_x/J)^{j+1}E_p^j-(\xi_x/J)^jE_p^{j-1}]+\mathfrak{D}\hat{q}^j \tag{30}$$

where we have used the fact that $\tilde{M}^j\hat{q}^j=0$, while on the right-hand side of Eq. (30), $\tilde{C}^j\hat{q}^j$, defined by Eq. (21a), was written in terms of the flux vectors. The delta form, in which the left-hand side operates on $\hat{q}^{j+1}-\hat{q}^j=\Delta\hat{q}^j$, is not as efficient as the nondelta version of the difference equation, Eq. (27). However, the delta form is more convenient in three dimensions, and, as discussed in Ref. 21, higher order spatial accuracy is easily obtained with the delta form algorithm.

Note that the flux vector $\hat{G}$ is not redefined to employ $p_s$ in the subsonic sublayer, because experience shows that no inconsistency develops in using the conventional definition of $\hat{G}$. We remark that $q$, not $E$, was used throughout as the dependent variable chiefly because it is awkward to express $G=CA^{-1}E$ in terms of the special sublayer flux vector $E_s$. Real gas effects and the viscous terms, especially the turbulent viscosity coefficients, are also more conveniently calculated in terms of $q$.

*4. Solution Procedure*

To advance the solution of Eq. (30), we first form the right-hand side terms, which require the flow variables only at the $j$ and $j-1$ levels, and then proceed to the implicit $\zeta$ sweep. The use of the central-difference approximation for the $\zeta$ derivatives on the left-hand side of Eq. (30) results in a block tridiagonal system of linear equations for the incremental flow variables, $\Delta\hat{q}^j_\ell$, $2 \le \ell \le \text{LMAX}-1$. The coefficients of the tridiagonal system are combinations of the $4\times4$ matrices $\bar{A}$, $\bar{C}$, and $\bar{M}$. A block-tridiagonal solver is used to obtain the incremental variables, and the new flow variables at the interior points are found using

$$\hat{q}^{j+1}_\ell = \hat{q}^j_\ell + \Delta\hat{q}^j_\ell \tag{31}$$

The application of the central-difference approximation at $\ell=2$ and $\ell=\text{LMAX}-1$ requires knowledge of $\Delta\hat{q}^j_{\ell=1}$ and $\Delta\hat{q}^j_{\ell=\text{LMAX}}$ on the boundaries. At the freestream boundary, the flow variables do not vary ($\Delta q=0$); thus $\Delta\hat{q}$ is dependent only on the $\xi$ variation of the metrics. At the body, the flow is governed by the no-slip and adiabatic wall boundary condition. Beam and Warming[13] have expended considerable effort in deriving an elegant implicit body-boundary condition scheme that maintains the proper order of accuracy.

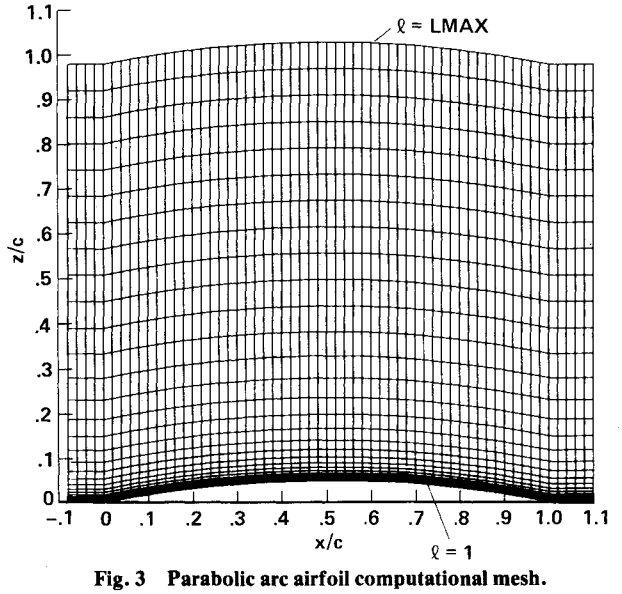


**Fig. 3 Parabolic arc airfoil computational mesh.**

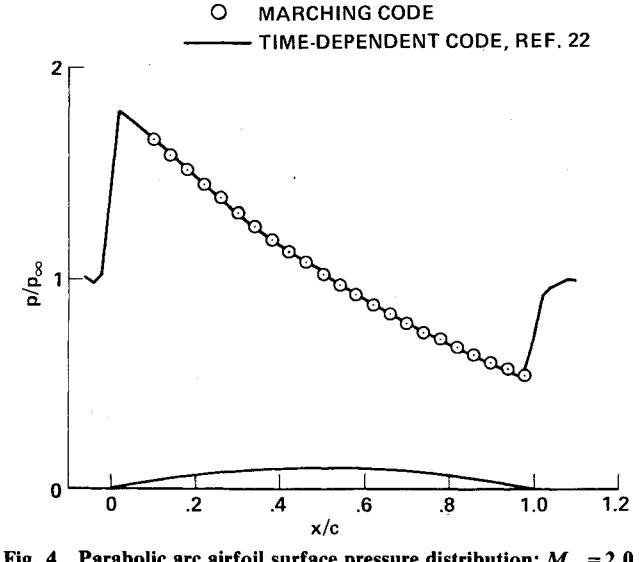


**Fig. 4 Parabolic arc airfoil surface pressure distribution; $M_\infty=2.0$, $Re_\infty=1.85\times10^6/c$ (turbulent).**

We have implemented their scheme but have also superseded it with a simpler scheme which yields almost identical results. At the body the no-slip condition gives $\Delta u^j_{\ell=1}=\Delta w^j_{\ell=1}=0$. The assumption that $p=p_s$ (i.e., $\partial p/\partial\zeta=0$) within the subsonic viscous layer is combined with the adiabatic wall condition, $\partial T/\partial\zeta=0$, to give $\partial\rho/\partial\zeta=0$. These are implemented as $\Delta p^j_{\ell=1}=\Delta p^j_{\ell=2}$, $\Delta\rho^j_{\ell=1}=\Delta\rho^j_{\ell=2}$, and combined with the known metric variation to determine $\Delta\hat{q}^j_{\ell=1}$. Although approximate, this scheme is accurate because it serves only as an approximation to $\Delta\hat{q}^j_{\ell=1}$ for the inversion step. After the flow variables are found at the interior points at $j+1$, the actual flow variables on the body at $j+1$ are determined from the three-point inward finite-difference approximations for $\partial p/\partial\zeta=0$ and $\partial\rho/\partial\zeta=0$ at the wall. Updating surface values of $p^{j+1}$ and $\rho^{j+1}$ from the boundary relations in this manner eliminates the accumulation of small errors due to the approximate implicit wall boundary condition.

### D. Two-Dimensional Results

Computations were made in order to verify the accuracy and versatility of the implicit marching algorithm. The test cases were chosen to duplicate steady flowfield results previously obtained from time-dependent computations using the Navier-Stokes code described by Steger.[22] The marching computations and the corresponding time-dependent cases were solved using identical grids, thus permitting a direct point-by-point comparison of the results as presented below.

The capacity of the marching code to handle streamwise variations of geometry was demonstrated by computing the flow over a nonlifting, 10% thick, parabolic arc airfoil. A turbulent flow was computed at $M_\infty=2.0$ and $Re_\infty=1.85\times10^6$ based on chord $c$ using the time-dependent code.[22] The computational grid is shown in Fig. 3. Flowfield profiles taken at $x/c=0.10$, $Re_x=0.185\times10^6$ were used as initial data for the marching code, and a marching solution was obtained for $0.10\le x/c\le1.0$.

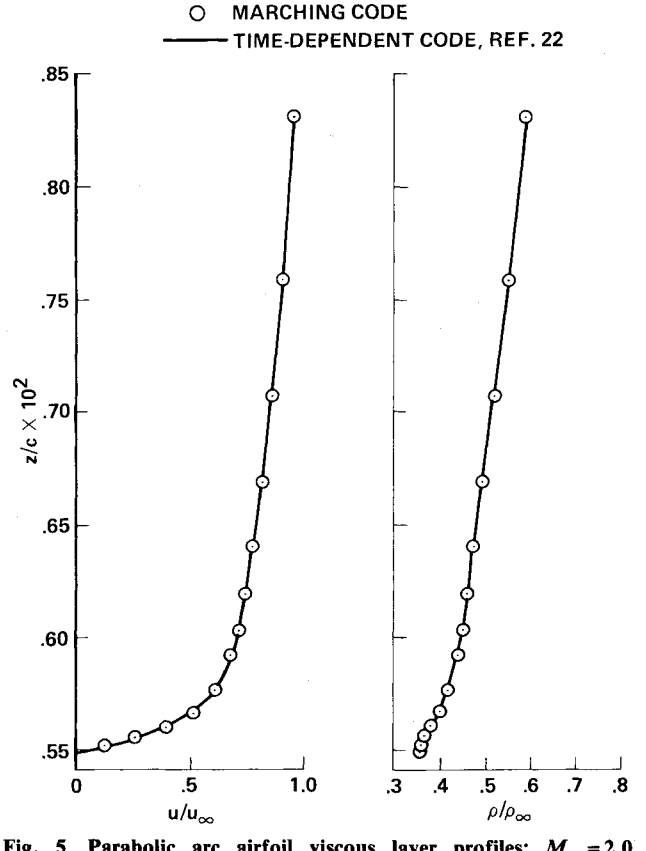


**Fig. 5 Parabolic arc airfoil viscous layer profiles; $M_\infty=2.0$, $Re_x=1.67\times10^6$ (turbulent), $x/c=0.90$.**

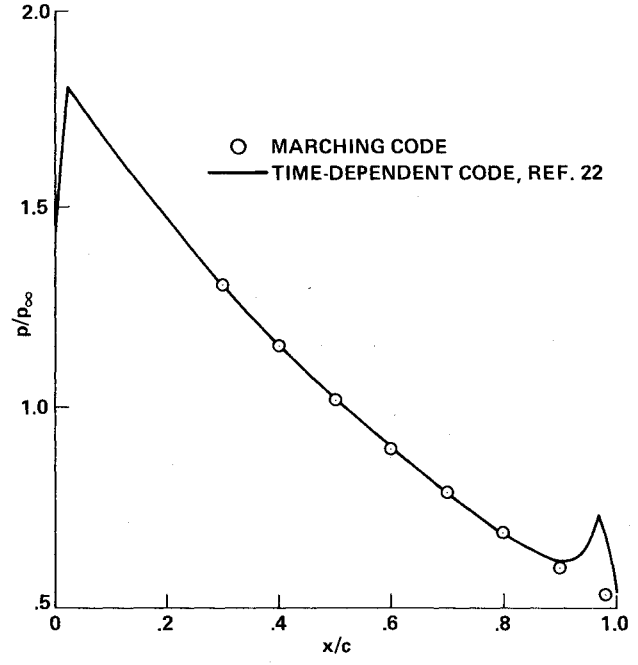


**Fig. 6 Parabolic arc airfoil surface pressure distribution; $M_\infty = 2.0$, $Re_\infty = 1.0 \times 10^6/c$ (laminar).**

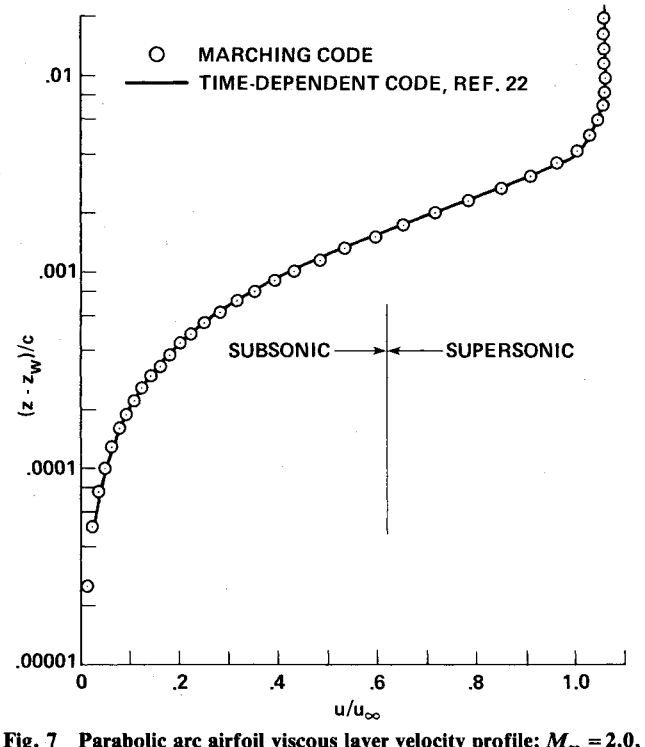


**Fig. 7 Parabolic arc airfoil viscous layer velocity profile; $M_\infty = 2.0$, $Re_x = 0.8 \times 10^6$ (laminar), $x/c = 0.8$.**

The marching and time-dependent surface-pressure distributions, shown in Fig. 4, demonstrate excellent agreement over the entire airfoil surface. Velocity and density profiles through the viscous layer at $x/c = 0.90$, $Re_x = 1.67 \times 10^6$, are shown in Fig. 5. Again, good agreement is observed between the marching and time-dependent results. This is not unexpected since, as has been discussed, the normal direction spatial-difference operators and the turbulence model of the marching code have the same form as those of the time-dependent code. In addition, the time-dependent results demonstrate that at each streamwise station, $\partial p/\partial \zeta = 0$ through the subsonic part of the viscous layer, physically justifying the validity of the viscous sublayer approximation made to permit marching.

### E. Departure Solutions and Global Iteration

The viscous subsonic layer method has proven to be both accurate and versatile. However, experience with the sublayer approximation shows that if one continues to refine the marching step size, $\Delta x$, far below what is usually required for accuracy, the method will ultimately diverge. This is not totally unexpected since the local linear analysis is only valid if $p_s$ is truly independent of $q$. The precise cause of the divergence, often called a departure solution, is not settled. An intriguing analysis by Lin and Rubin[3] suggests that disturbances can amplify when certain integral quantities across the subsonic layer are negative, but it is not clear, at least to us, that their analysis sufficiently models the process of impressing $p_s$ from the stable supersonic region. In any event, we find that the departure-solution behavior can be controlled by using a global-iteration process similar to one commonly used in boundary-layer theory.

In the global iteration technique one initially specifies an entire $p_s$ distribution. The subsonic layer marching method (with $p_s$ specified) is then used as part of a relaxation procedure to predict a new flowfield solution and a new $p_s$ distribution. The new $p_s$ distribution is then used to obtain an improved solution, and so on until the new wall shear stress equals that of the previous iteration. Because $p_s$ is specified, any small value of $\Delta x$ can be used in the marching scheme.

A good initial guess for $p_s$ can be obtained by running the usual sublayer marching procedure with a sufficiently large value of $\Delta x$ to be stable. Alternatively, a constant value of $p_s$, corresponding to $\partial p_s/\partial \xi = 0$, can be safely used as an initial guess. Experience with the global iteration technique shows that 1) the solutions obtained with the viscous sublayer method for stable values of $\Delta x$ are usually accurate, and 2) that even if a poor estimate of $p_s$ is initially specified, the global-iteration process is rapidly convergent. In most cases, the pressure distribution is converged after two iterations, and the skin-friction distribution no longer varies after three or four iterations.

The following computations illustrate the additional stability gained from the global-iteration process. The surface-pressure distribution for laminar viscous flow over a 10% thick biconvex airfoil at $M_\infty = 2.0$ and $Re_\infty = 1.0 \times 10^6$ based on chord, is shown in Fig. 6. This solution was computed using the time-dependent code of Ref. 22. The corresponding velocity profile through the viscous layer at $x/c = 0.8$ is shown in Fig. 7. A marching solution, obtained using the subsonic layer approximation for $p_s$ and using $\Delta x = 0.020$, is also shown in Figs. 6 and 7. The results are in excellent agreement with the time-dependent solution and one should note that in this example some 23 points are within the subsonic sublayer. The marching solution obtained for $\Delta x = 0.010$ is identical to that for $\Delta x = 0.020$, but when $\Delta x = 0.005$ was attempted, the solution diverged. However, by using the global iteration procedure with $p_s$ initially constant, rapidly convergent solutions (identical to the one obtained for $\Delta x = 0.010$) are obtained for the smaller step sizes, $\Delta x = 0.005$ and $\Delta x = 0.00125$. The convergence sequence for the wall shear stress distribution over the first three iterations of the $\Delta x = 0.00125$ case is shown in Fig. 8.

## III. Three-Dimensional Flow

The development of the implicit marching algorithm for steady three-dimensional flow closely parallels the one just presented for two-dimensional flow. The same physical assumptions are made, specifically, neglecting the streamwise derivatives within the viscous terms, and using the sublayer approximation. The inclusion of the additional spatial coordinate leads to a factored sequence of block-tridiagonal equations, whose block coefficients are now $5 \times 5$ matrices.

In this section, we merely outline the development of the three-dimensional algorithm, because the extension from two-dimensions is straightforward.

### A. Transformed Governing Equations

The three-dimensional steady Navier-Stokes equations, written in nondimensional form,[17] are

$$\frac{\partial \hat{E}}{\partial \xi}+\frac{\partial \hat{F}}{\partial \eta}+\frac{\partial \hat{G}}{\partial \zeta}=\frac{1}{Re}\left(\frac{\partial \hat{R}}{\partial \xi}+\frac{\partial \hat{T}}{\partial \eta}+\frac{\partial \hat{S}}{\partial \zeta}\right) \tag{32}$$

where

$\xi=\xi(x)$ = streamwise coordinate

$\eta=\eta(x,y,z)$ = spanwise (circumferential) coordinate

$\zeta=\zeta(x,y,z)$ = normal coordinate

Here the body is assumed to be mapped onto the $\zeta=0$ plane (see Fig. 9). As before, we neglect the streamwise derivatives within the viscous terms of Eq. (32). This approximation is physically valid for high Reynolds number flows, where streamwise flow gradients within the subsonic viscous layer are negligible in comparison to those in the normal direction. The same argument permits us also to neglect viscous derivatives along the body in the circumferential direction.

Although it is not necessary to drop the circumferential viscous terms in the development of the parabolized Navier-Stokes approximation, doing so simplifies the computations and is therefore incorporated in the present work. The remaining viscous terms, containing only normal derivatives, constitute the thin-layer model (cf., Refs. 19, 22, and 23 for further discussion) and can be written as $(1/Re)\partial\hat{S}/\partial\zeta$, where $\hat{S}$ is similar to Eq. (8) and is defined in Ref. 21. Introducing the sublayer approximation, the resulting three-dimensional parabolized Navier-Stokes equations can be written as

$$\frac{\partial \hat{E}_s}{\partial \xi}+\frac{\partial \hat{F}}{\partial \eta}+\frac{\partial \hat{G}}{\partial \zeta}=\frac{1}{Re}\frac{\partial \hat{S}}{\partial \zeta} \tag{33}$$

The inviscid flux vectors in Eq. (33), the thin-layer model viscous term, and the Jacobian matrices all parallel their two-dimensional counterparts and are defined in Ref. 21.

### B. Numerical Algorithm and Solution Procedure

The implicit marching algorithm for the solution of Eq. (33) is derived in the same manner as its two-dimensional counterpart, with the $\hat{F}$ flux vector linearized in the same manner as $\hat{G}$. The resulting algorithm, written in delta form, is

$$\begin{aligned}&[\tilde{A}_s^j+(1-\alpha)\Delta\xi(\delta_\eta\tilde{B}^j+\delta_\zeta\tilde{C}^j-Re^{-1}\delta_\zeta\tilde{M}^j)](\hat{q}^{j+1}-\hat{q}^j)\\&=-(\tilde{A}_s^j-\tilde{A}_s^{j-1})\hat{q}^j+\alpha(\hat{E}_s^j-\hat{E}_s^{j-1})-(1-\alpha)\Delta\xi\\&\times\{\delta_\eta[\eta_x^{j+1}(E/J)^j+\eta_y^{j+1}(F/J)^j+\eta_z^{j+1}(G/J)^j]\\&+\delta_\zeta[\zeta_x^{j+1}(E/J)^j+\zeta_y^{j+1}(F/J)^j+\zeta_z^{j+1}(G/J)^j]\\&-Re^{-1}\delta_\zeta\tilde{S}^j\}-[(\xi_x/J)^{j+1}E_p^j-(\xi_x/J)^jE_p^{j-1}]+\mathfrak{D}\hat{q}^j\end{aligned} \tag{34}$$

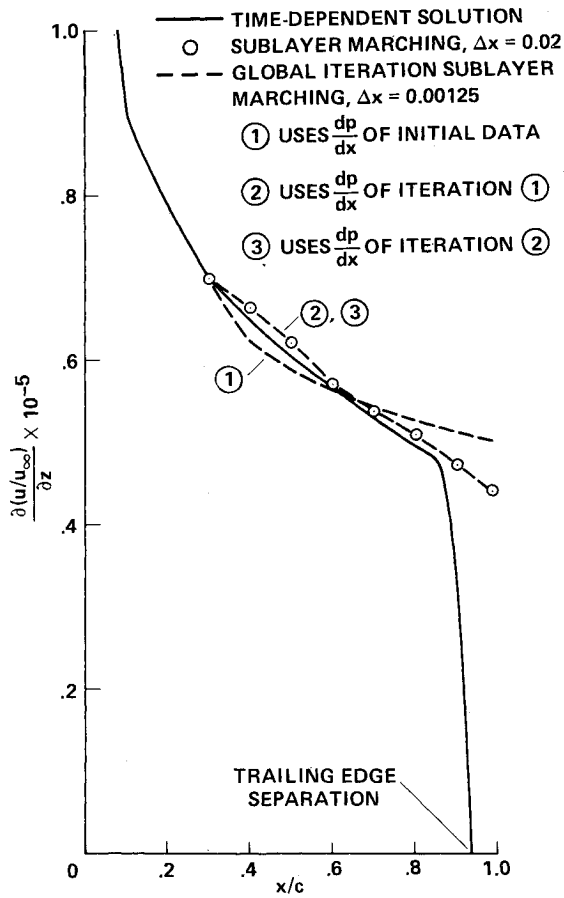


**Fig. 8 Velocity gradient distribution on parabolic arc airfoil illustrating global iteration procedure.**

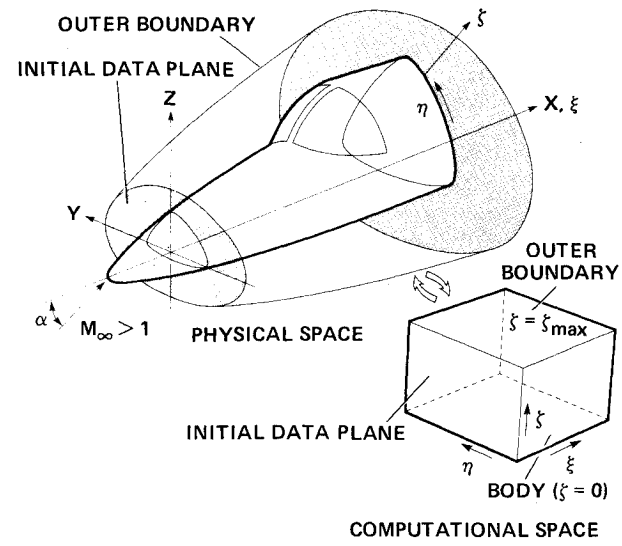


**Fig. 9 Transformation of physical space into computational space.**

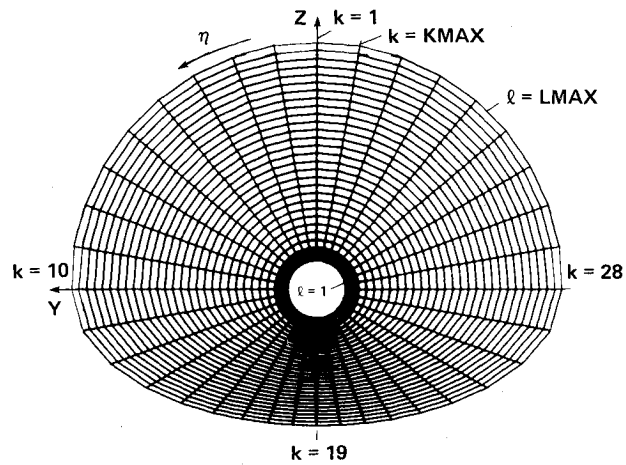


**Fig. 10 Cross section of typical computational grid, $x=x_0(\xi_0)$.**

where $\delta_\eta$ is central differenced like $\delta_\xi$, Eq. (16), and the smoothing term $\mathfrak{D}$ is defined by

$$\mathfrak{D}=\epsilon_e\tilde{A}^j_{s_{k,\ell}}\left(\frac{1}{J}\right)^j[(\nabla_\eta\Delta_\eta)^2(J\hat{q})^j+(\nabla_\xi\Delta_\xi)^2(J\hat{q})^j]$$

Here $\epsilon_e$ must be less than 1/16 for stability.

An approximately-factored form of Eq. (34), which retains the same order of accuracy in $\xi$, can be obtained if we note that

$$[\tilde{A}^j_s+(1-\alpha)\Delta\xi(\delta_\eta\tilde{B}^j)](\tilde{A}^j_s)^{-1}[\tilde{A}^j_s+(1-\alpha)\Delta\xi(\delta_\xi\tilde{C}^j$$
$$-Re^{-1}\delta_\xi\tilde{M}^j)]\Delta\hat{q}^j=\text{LHS(34)}+0(\Delta\xi)^3 \qquad (35)$$

(Note: $A_s^{-1}$ can degrade the factorization error if $u$ is sufficiently small.) Upon replacing the left-hand side of Eq. (34), LHS(34), with the left-hand side of Eq. (35), one obtains the factored algorithm. The algorithm is solved by the sequence of implicit inversions

$$[\tilde{A}^j_s+(1-\alpha)\Delta\xi(\delta_\eta\tilde{B}^j)]\Delta\hat{q}_*=\text{RHS(34)} \qquad (36a)$$

$$[\tilde{A}^j+(1-\alpha)\Delta\xi(\delta_\xi\tilde{C}^j-Re^{-1}\delta_\xi\tilde{M}^j)]\Delta\hat{q}^j=\tilde{A}^j_s\Delta\hat{q}_* \qquad (36b)$$

Equation (36) differs from its two-dimensional analogy primarily in the inclusion of the implicit circumferential inversion factor.

A typical computational grid is shown in the physical crossflow plane $[x=x_0(\xi_0)]$ in Fig. 10. The grid extends radially between the body surface and an outer boundary located in the undisturbed freestream, and is chosen to completely circumscribe the body, $1\le k\le$KMAX, to permit a treatment of nonbilaterally-symmetric flows. Such flows include the case of combined angles of attack and yaw, and the important case of a nonsymmetric leeward side wake exhibited by axisymmetric bodies at large incidence. Symmetric flows can be treated with half the computational effort by employing a grid that runs from the windward to leeward plane of symmetry and by applying the usual symmetry conditions at the edges.

To advance the solution of Eq. (36), we first form the right-hand-side terms of Eq. (36a) and perform the circumferential implicit inversion. The use of a central-difference approximation for the $\eta$ derivatives, together with the periodic continuation condition, leads to a periodic block-tridiagonal system of equations. This system is inverted, using the solver described in Ref. 24, to obtain the intermediate variables. Once these quantities are known, the right-hand-side terms of Eq. (36b), $\tilde{A}^j_s\Delta\hat{q}_*$, are evaluated, and the equation is inverted in the normal direction, using the same procedure previously described for Eq. (30), to obtain $\Delta\hat{q}^j_{k,\ell}$, and thus $\hat{q}^{j+1}_{k,\ell}$.

### C. Three-Dimensional Results

The accuracy of the factored marching algorithm applied to three-dimensional flow was evaluated by computing the flowfield about a hemisphere-cylinder body both at 0 and 5 deg angle of attack. The test-case conditions were again chosen to duplicate steady flowfield results obtained from time-dependent Navier-Stokes computations and, for the body at incidence, to match those of the wind-tunnel experiment described in Ref. 25.

#### *1. Axisymmetric Flow*

Although the flowfield surrounding the hemisphere cylinder at zero incidence is axisymmetric, the Cartesian velocity components used in the computation vary sinusoidally in the circumferential direction around the body. Thus, this case provides a nontrivial test of the factorization procedure. The azimuthal-invariant, time-dependent code, described in Ref. 26, was used to compute the turbulent flow around the body at $M_\infty=2.0$ and $Re_\infty=8.80\times10^4$ based on nose radius $R_N$. The flowfield exhibits an embedded subsonic region in the shock layer at the nose, which expands around the nose and becomes supersonic in the vicinity of the sphere-cylinder junction. Flow profiles taken at $x/R_N=3.45$, downstream of the subsonic region, were used as initial data for the marching code, and a marching solution was obtained for $3.45\le x/R_N\le21.0$.

The marching and time-dependent surface-pressure distributions are shown in Fig. 11 and are in good agreement over the entire body. The small axial oscillation in the marching results is attributed to a small inconsistency between the initial data and the marching technique. The amplitude of the oscillation is never more than 1% of the pressure and is seen to damp toward the rear of the body. Velocity and density profiles within the viscous layer, taken from the marching and

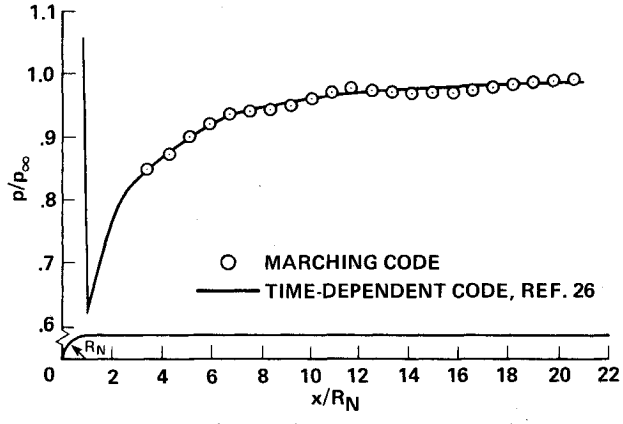


**Fig. 11 Axisymmetric hemisphere cylinder surface pressure distribution; $M_\infty=2.0$, $Re_\infty=8.80\times10^4/R_N$ (turbulent).**

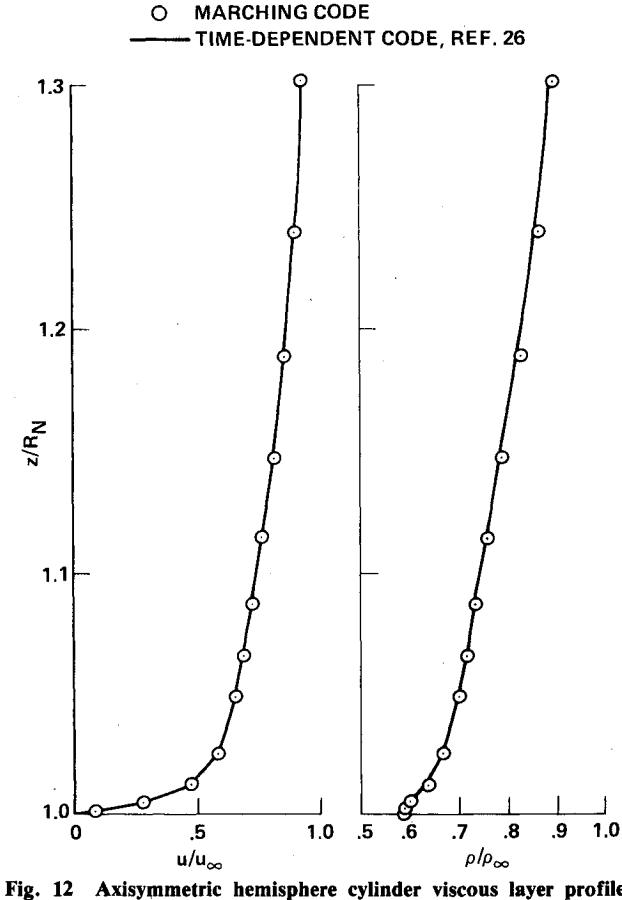


**Fig. 12 Axisymmetric hemisphere cylinder viscous layer profiles; $M_\infty=2.0$, $Re_x=1.81\times10^5$ (turbulent), $x/R_N=20.6$.**

time-dependent solutions at $x/R_N = 20.6$, are shown in Fig. 12. The marching results show good agreement with those of the time-dependent code.

*2. Hemisphere Cylinder at Incidence*

The flowfield surrounding a hemisphere cylinder at incidence in a low Mach number supersonic stream has recently been investigated experimentally by Hsieh,[25] and computationally by Pulliam and Steger,[23] who used a three-dimensional, time-dependent, thin-layer Navier-Stokes code. Their computational grid was selected to resolve the details of the flow in the region of the nose, and in this region the computed results are in good agreement with the experimental measurements. However, the limitation of computer storage required that the grid be progressively stretched axially along the cylinder. Consequently, the streamwise details of the downstream flow were only marginally resolved. The use of the marching code, with initial data taken from the time-dependent solution in a region of good resolution, can circumvent the storage limitations. A steady turbulent flow solution was obtained using the time-dependent code,[23] at $M_\infty = 1.40$, $Re_\infty = 2.0 \times 10^5$ based on $R_N$, and $\alpha = 5$ deg. Data taken at $x/R_N = 3.07$ were prescribed as initial data and a marching solution was obtained from $3.07 \le x/R_N \le 40.0$. A comparison of the surface-pressure distributions along the windward and leeward planes of symmetry is shown in Fig. 13, together with the experiments of Hsieh.[25] Although the marching solution was obtained for $x/R_N \le 40.0$, and could be continued downstream, only the data for the region where the marching results, the time-dependent results, and the experimental measurements overlap, $3.07 \le x/R_N \le 16.0$, are presented in Fig. 13. The marching results are in good agreement with the time-dependent results in the region common to both computations, $x/R_N \le 14.0$, and both are in good agreement with the measured surface pressures. However, the marching-code results give better agreement with the measured values for $9.0 \le x/R_N \le 14.0$, where the time-dependent solution lacks resolution.

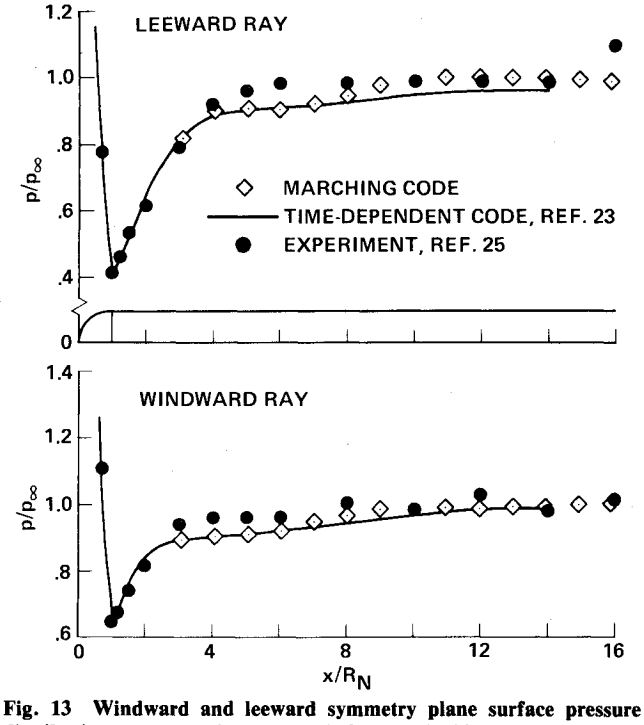


**Fig. 13 Windward and leeward symmetry plane surface pressure distributions on hemisphere cylinder at incidence; $M_\infty = 1.40$, $Re_\infty = 2.0 \times 10^5/R_N$ (turbulent), $\alpha = 5$ deg.**

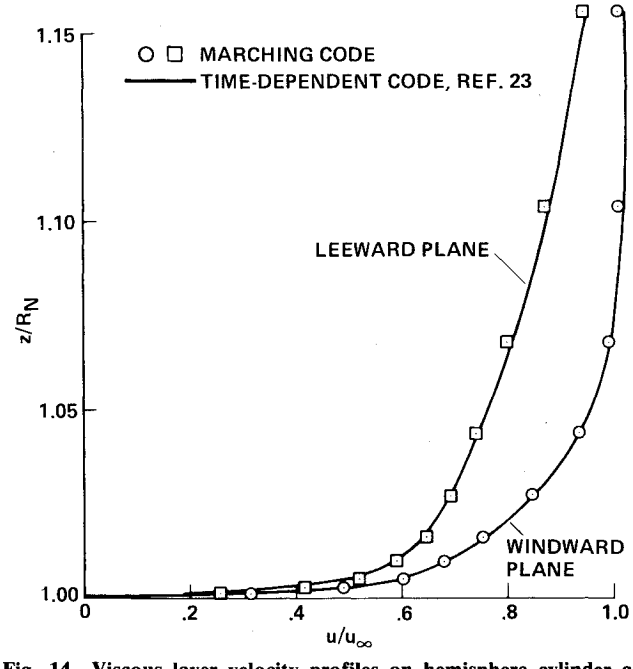


**Fig. 14 Viscous layer velocity profiles on hemisphere cylinder at incidence; $M_\infty = 1.40$, $Re_x = 1.40 \times 10^6$ (turbulent), $x/R_N = 6.98$, $\alpha = 5$ deg.**

Streamwise velocity profiles through the viscous layer on the windward and leeward rays, taken from the computational results at $x/R_N = 6.98$, are shown in Fig. 14. At this axial location, the stretched grid of the time-dependent solution still maintains adequate streamwise resolution. The velocity gradient is much more sensitive than is surface pressure. Thus, the good agreement between the time-dependent and the marching solutions attests to the accuracy of the factored marching algorithm. Also, the time-dependent results exhibit constant pressure across the subsonic viscous layer, thus justifying the assumptions made in the viscous sublayer approximation.

## IV. Summary

A noniterative, implicit, finite-difference marching algorithm has been developed for steady, supersonic viscous flow. The parabolized Navier-Stokes equations, in strong conservation law form, have been transformed into general coordinates so that arbitrary body shapes can be mapped onto constant planes in the uniform computational space. The approximately-factored finite-difference algorithm is noniterative, second-order accurate in the marching direction, and second- or fourth-order accurate in the crossflow plane. Use of the subsonic layer approximation with a global iteration technique for "surface" pressure allows the grid spacing to be refined in a uniform manner.

## References

[1] Cheng, H. K., Chen, S. Y., Mobley, R., and Huber, C. R., "The Viscous Hypersonic Slender-Body Problem: A Numerical Approach Based on a System of Composite Equations," RM 6193-PR, The Rand Corp., Santa Monica, Calif., May 1970.

[2] Rubin, S. G. and Lin, T. C., "Numerical Methods for Two- and Three-Dimensional Viscous Flow Problems: Application to Hypersonic Leading Edge Equations," PIBAL Rept. 71-8 (AFOSR-TR-71-0778), 1971.

[3] Lin, T. C. and Rubin, S. G., "Viscous Flow Over a Cone at Moderate Incidence: I Hypersonic Tip Region," *Computers and Fluids*, Vol. 1, 1973, pp. 37-57.

[4] Nardo, C. T. and Cresci, R. J., "An Alternating Directional Implicit Scheme for Three-Dimensional Hypersonic Flows," *Journal of Computational Physics*, Vol. 8, 1971, pp. 268-284.

[5] Lubard, S. C. and Helliwell, W. S., "Calculation of the Flow on a Cone at High Angle of Attack," *AIAA Journal*, Vol. 12, July 1974, pp. 965-974.

[6] Vigneron, Y. C., Rakich, J. V., and Tannehill, J. C., "Calculation of Supersonic Viscous Flow Over Delta Wings with Sharp Subsonic Leading Edges," AIAA Paper 78-1137, 1978.

[7] Patankar, S. V. and Spalding, D. B., "A Calculation Procedure for Heat, Mass and Momentum Transfer in Three-Dimensional Parabolic Flows," *International Journal of Heat Mass Transfer*, Vol. 15, 1972, pp. 1787-1806.

[8] McDonald, H. and Briley, W. R., "Three-Dimensional Supersonic Flow of a Viscous or Inviscid Gas," *Journal of Computational Physics*, Vol. 19, 1975, pp. 150-178.

[9] Briley, W. R., "Numerical Method for Predicting Three-Dimensional Steady Viscous Flow in Ducts," *Journal of Computational Physics*, Vol. 14, 1974, pp. 8-28.

[10] Kreskovsky, J. P. and Shamroth, S. J., "An Implicit Marching Method for the Two-Dimensional Reduced Navier-Stokes Equations at Arbitrary Mach Number," *Computer Methods in Applied Mechanics and Engineering*, Vol. 13, 1978, pp. 307-334.

[11] Roberts, D. W. and Forester, C. K., "A Parabolic Computational Procedure for Three-Dimensional Flows in Ducts with Arbitrary Cross Section," AIAA Paper 78-143, 1978.

[12] Birch, S. F., Paynter, G. C., Spalding, D. B., and Tatchell, D. G., "Numerical Modeling of Three-Dimensional Flows in Turbofan Engine Exhaust Nozzles," *Journal of Aircraft*, Vol. 15, Aug. 1978, pp. 489-496.

[13] Beam, R. and Warming, R. F., "An Implicit Factored Scheme for the Compressible Navier-Stokes Equations," *AIAA Journal*, Vol. 16, April 1978, pp. 393-402.

[14] Warming, R. F. and Beam, R., "On the Construction and Application of Implicit Factored Schemes for Conservation Laws," *SIAM-AMS Proceedings of the Symposium on Computational Fluid Mechanics*, Vol. 11, New York, 1977.

[15] Rudman, S. and Rubin, S. G., "Hypersonic Viscous Flow over Slender Bodies with Sharp Leading Edges," *AIAA Journal*, Vol. 6, Oct. 1968, pp. 1883-1890.

[16] Davis, R. T., "Numerical Solutions of the Hypersonic Viscous Shock-Layer Equations," *AIAA Journal*, Vol. 8, May 1970, pp. 843-851.

[17] Peyret, R. and Viviand, H., "Computations of Viscous Compressible Flows Based on the Navier-Stokes Equations," AGARD-AG-212, 1975.

[18] Viviand, H., "Conservative Forms of Gas Dynamic Equations," *La Recherche Aerospatiale*, No. 1, Jan.-Feb. 1974, pp. 65-68.

[19] Baldwin, B. S. and Lomax, H., "Thin Layer Approximation and Algebraic Model for Separated Turbulent Flows," AIAA Paper 78-257, 1978.

[20] Steger, J. L., "Coefficient Matrices for Implicit Finite Difference Solution of the Inviscid Fluid Conservation Law Equations," *Computer Methods in Applied Mechanics and Engineering*, Vol. 13, 1978, pp. 175-188.

[21] Schiff, L. B. and Steger, J. L., "Numerical Simulation of Steady Supersonic Viscous Flows," AIAA Paper 79-130, 1979 (also NASA TP-1749, 1981).

[22] Steger, J. L., "Implicit Finite-Difference Simulation of Flow About Arbitrary Two-Dimensional Geometries," *AIAA Journal*, Vol. 16, July 1978, pp. 679-686.

[23] Pulliam, T. H. and Steger, J. L., "On Implicit Finite-Difference Simulations of Three-Dimensional Flow," AIAA Paper 78-10, 1978.

[24] Steger, J. L., "Implicit Finite-Difference Simulation of Flow About Arbitrary Geometries with Applications to Airfoils," AIAA Paper 77-665, 1977.

[25] Hsieh, T., "An Investigation of Separated Flow About a Hemisphere-Cylinder at 0- to 19-Deg Incidence in the Mach Number Range from 0.6 to 1.5," AEDC-TR-76-112, Nov. 1976.

[26] Nietubicz, C. J., Pulliam, T. H., and Steger, J. L., "Numerical Solution of the Azimuthal-Invariant Thin-Layer Navier-Stokes Equations," AIAA Paper 79-10, 1979.